Electronic Supporting Information (ESI)

for

A multi-scale molecular dynamics study of the assembly of micron-size supraparticles from 30 nm alkyl-coated nanoparticles

Damien Thompson,*[a] Mateusz Sikora,[b] Piotr Szymczak,[c] and Marek Cieplak[b]

[a] Theory, Modelling and Design Centre, Tyndall National Institute, University College Cork, Cork, Ireland. Tel:+353214904063. [b]Institute of Physics, Polish Academy of Sciences, Al. Lotnikow 32/46, 02-668 Warsaw, Poland. [c]Institute of Theoretical Physics, Faculty of Physics, University of Warsaw, ul Hoza 69, 00-681 Warsaw, Poland.

*Corresponding author: damien.thompson@tyndall.ie

S1 – Detailed simulation methods

S1.1. Detailed methods for the atomistic simulations: Periodic boundary conditions were applied, meaning the primary simulation cell was replicated periodically in all directions, and Ewald summation[1] was used to calculate all electrostatic interactions. Each model was subjected to ten nanoseconds (10 ns) of molecular dynamics to allow formation of well-equilibrated, room temperature structures. This corresponds to 0.42 microseconds of dynamics overall, composed of 70 ns for equilibration plus 350 ns of equilibrated dynamics (see main text Methods for the details of the 35 models). The CHARMM[2] and NAMD[3] input scripts used for the simulations, together with the computed structures, are available on request from the corresponding author.

The forms of the Morse potentials[4] used to fit the MD interaction energies are given in Table S1 below. von Lilienfeld and Andrienko[4] analyzed different forms of potentials for interactions between (in this case, polyaromatic) hydrocarbons and found that the Morse potential best reproduces the repulsive and the attractive part of the potential, validated with respect to density functional theory.

Table S1. Morse potential equations and parameters used to fit the calculated interaction energies.

Figure No.	Fitting equation	Parameters
Fig. 2a	$V = \varepsilon\left(1 - e^{-a(x-r_0)}\right)^2 - \varepsilon_0$	$\varepsilon = 0.009$, $a = 0.969$, $r_0 = 2.035$, $\varepsilon_0 = 1.080$
Fig. 4a	$V = \varepsilon\left(1 - e^{-a(x-r_0)}\right)^2 - \varepsilon_0$	$\varepsilon = 0.053$, $a = 2.200$, $r_0 = 2.650$, $\varepsilon_0 = 1.145$
Fig. S1a (black)	$V = \varepsilon\left(1 - e^{-a(x-r_0)}\right)^2 - \varepsilon_0$	$\varepsilon = 0.252$, $a = 2.603$, $r_0 = 4.003$, $\varepsilon_0 = 1.345$
Fig. S1a (red)	$V = \varepsilon\left(1 - e^{-a(x-r_0)}\right)^2 - \varepsilon_0$	$\varepsilon = 0.280$, $a = 2.581$, $r_0 = 3.996$, $\varepsilon_0 = 1.372$
Fig. S3a	$V = \varepsilon\left(1 - e^{-a(x-r_0)}\right)^2 - \varepsilon_0$ $+ \dfrac{b}{\left(\cosh\left(\dfrac{x-r_1}{d}\right)\right)^2}$	$\varepsilon = 0.092$, $a = 7.381$, $r_0 = 2.150$, $\varepsilon_0 = 1.331$, $b = 0.074$, $r_1 = 2.300$, $d = 0.135$

Fits are shown for the MD interaction energy datasets in the Figures as given in main text and in section S2.

S1.2. Detailed methods for the mesoscopic simulations: As described in the main text Results for the atom-scale simulations, the energy scales involved in the particle-particle interactions are large compared to room temperature thermal energies, $k_B T \sim 26$ meV, where k_B is Boltzmann's constant and T is the absolute temperature. We perform our simulations at the reduced temperature of $T^* = k_B T / \varepsilon_{NP-NP}$ of 0.001, where ε is a characteristic depth of the energy well. Note also that $\varepsilon_{NP-wall}$ is approximately 4 times stronger than ε_{NP-NP}, as defined from the atomistic potentials and represented using a 3-9 potential.[5] (See pages S13-S15 below for control simulations at elevated temperatures.)

For Brownian dynamics[6] the displacement of the i-th nanoparticle, Δr_i, at timestep Δt is given by

$$\Delta r_i = \frac{1}{k_B T} D F_i \Delta t + B_i \qquad \text{Equation 1}$$

where $\boldsymbol{B}_i$ is a Gaussian distributed random displacement with $< \boldsymbol{B}_i > = 0$ and $< \boldsymbol{B}_i \boldsymbol{B}_i > = 2D\mathbf{1}\Delta t$.

D denotes the diffusion constant, equal to

$$D = \frac{k_B T}{6\pi\eta R_{NP}}$$ Equation 2

using the the Stokes-Einstein relation for spherical particles[7], where η denotes viscosity and R_{NP} is the nanoparticle radius. We impose an external field $\boldsymbol{F}$ (Equation 1) to push the NPs towards the surface.

Note that there are no explicit water molecules in the simulations. This type of Brownian dynamics is a fairly common way to account for the solvent in an implicit way, as introduced by Ermak and McCammon.[6] Instead of molecules of the solvent we have an effective medium that provides random forces and drag forces.

S2 – Control simulations

S2.1 Molecular dynamics of the interface between coated flat surfaces: Self-assembled monolayers (SAMs) of alkanethiol molecules on flat Au(111) serve as a model for surfaces with zero curvature (or, towards the limit of infinitely large nanoparticles). The derived energy *vs.* separation potential in Figure S1a shows that a gap separation of 4.0 nm between surfaces is preferred, with monolayers on opposing faces stacking to form a bilayer. Figure S1a shows that the approach geometry in which the molecules on opposing surfaces have aligned, rather than juxtaposed, tilt angles[8-10] is more favourable and so this approach geometry is used for all the interaction calculations. The error bars denote the time-averaged uncertainties in the energies and are similarly small for both flat surfaces and 30 nm particles (averaging at 0.004 and 0.002 eV/molecule in Figure S1a and main text Figure 2a respectively).

Radial distribution functions (RDFs) in Figure S1b show how this 4.0 nm separation gives optimum contacts between terminal methyl groups at the interface between the two surfaces. As shown in Figure S1b, at 4.0 nm (black curve), the H---H contacts between chains on opposing faces are

centered at the target force field distance of 0.264 nm derived from *ab intio* electronic structure calculations and experiments.[2] The 0.1 nm nearer (blue curve) and 0.1 nm further (gold curve) separations skew the distribution to less favourable, respectively repulsive and only weakly attractive H---H distances (see also main text Figure 2b and discussion in the main text). The lack of interdigitation between chains on opposing faces is due to the tight packing between chains along each flat Au(111) surface.[9-10] This gives a steep potential well in Figure S1a, with penalties for chain-chain interactions on the order of 0.22 and 0.14 eV/nm for separations of 3.9 and 4.1 nm, with even steeper chain penalties of 0.60 and 0.36 eV/nm for further deviations to 3.8 and 4.2 nm. Penalties are higher as expected for sub-4.0 nm separations due to repulsive van der Waals contacts.

The alternative model with chains juxtaposed at the interface gives a similar shaped potential as shown in Figure S1a, but with a higher-lying minimum that is shifted upwards by 0.02 eV/chain, reflecting the mismatch between chains on the opposing faces. The chain energies in both models converge to the same asymptotic value of -1.24 eV at the large separation of 4.4 nm as the hexadecanethiol chain packing energy in each monolayer of approximately -1.3 eV[9-10] predominates the energy, with a negligible contribution from the (now largely dissociated) interface.
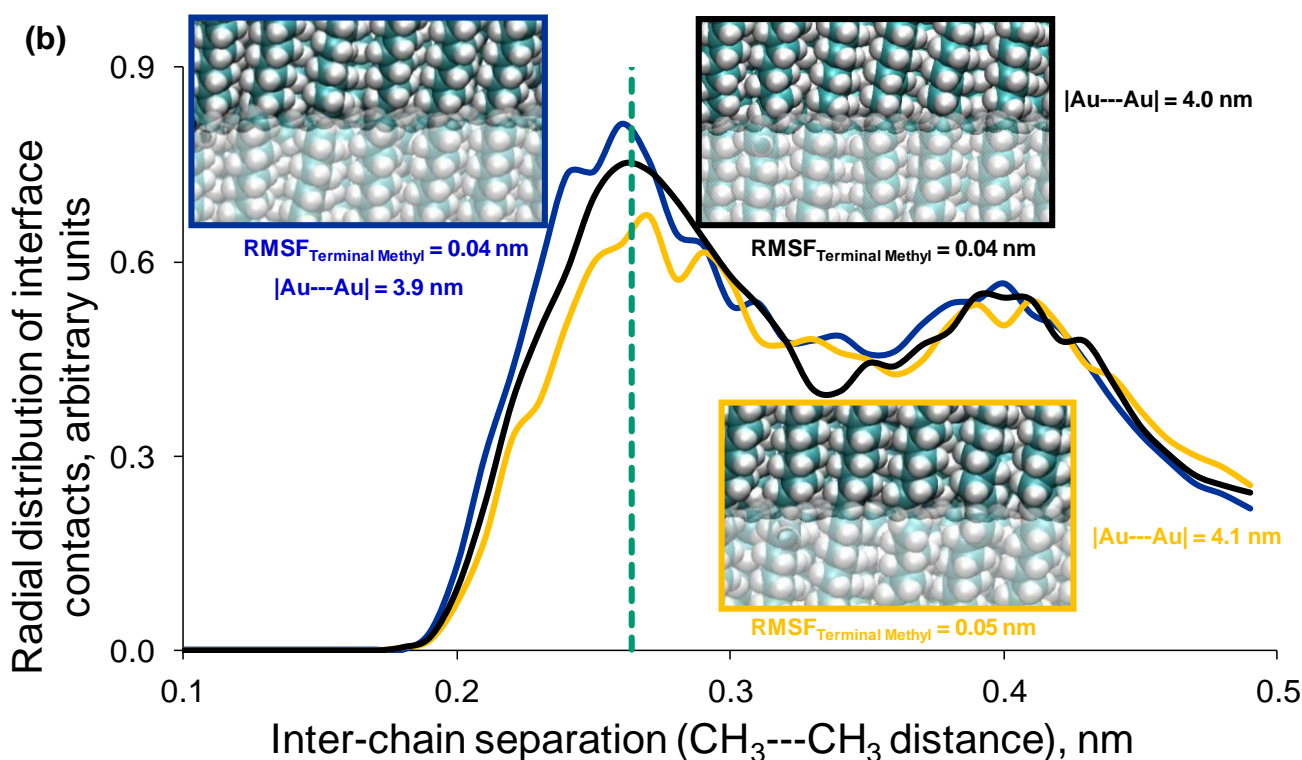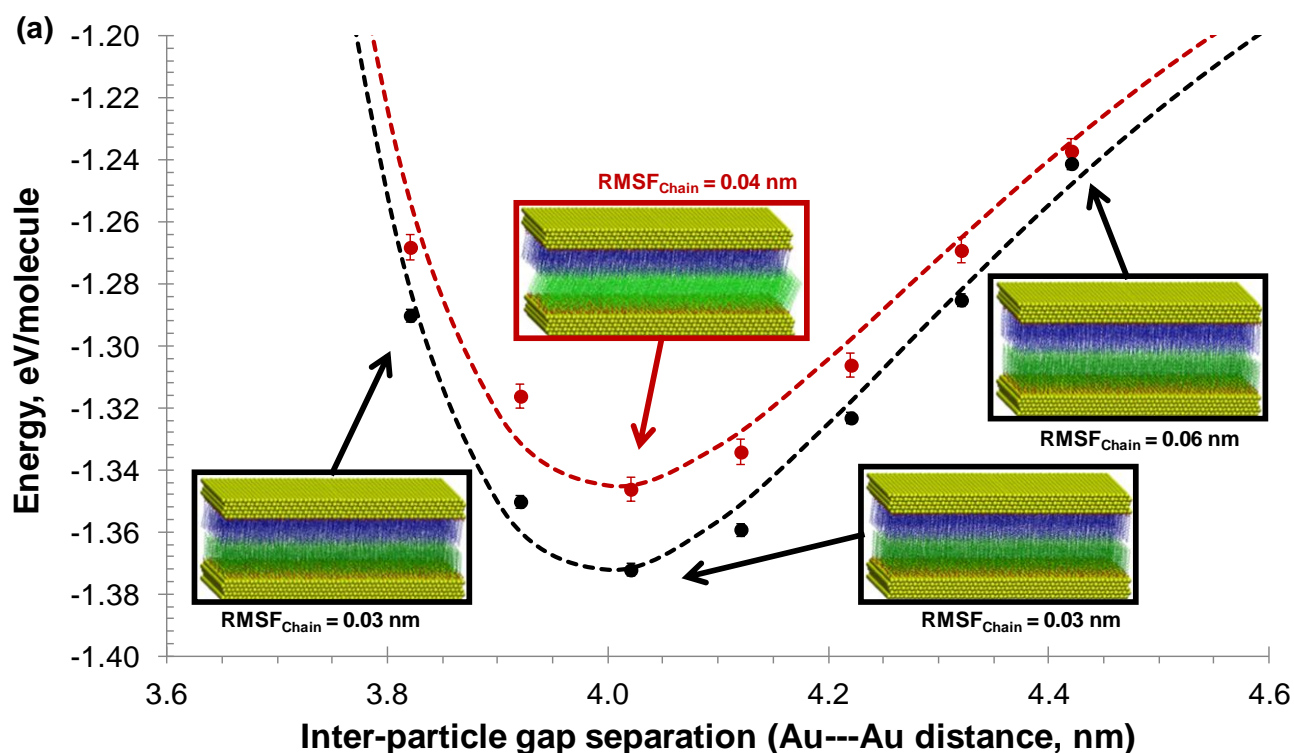
Figure S1. (a) Interaction energy (eV per molecule) *vs.* gap separation (nm) for flat, hexadecanethiol-coated gold surfaces. Data for bilayers with aligned and juxtaposed monolayer tilt angles are coloured black and red respectively, with error bars on each point showing the standard deviation over 200 molecular dynamics structures (sampling every 10 ps over the final 2 ns of dynamics). Representative molecular dynamics structures, together with time-averaged root mean square fluctuations (RMSF) for chains are given in the inset panels; Au atoms are shown as van der Waals's spheres, thiol anchor groups are shown as small red spheres and alkyl chains are shown as sticks, coloured blue and green to distinguish between chains on

each face, with hydrogen atoms omitted for clarity. **(b)** Radial distribution functions (RDF) for contacts between terminal methyl groups on each face. In this case the molecular dynamics structures show the chain structure at the interface, with carbon and hydrogen atoms shown as light blue and white spheres and one monolayer made partially transparent to distinguish between layers. The blue, black and gold curves show RDFs for interfaces constructed from 3.9, 4.0 and 4.1 nm gold---gold separations as marked in the top panel, and the dashed green line marks the target 0.264 nm H---H separation[2] at the interface.

The measured time-averaged root mean square fluctuation (RMSF) values in Figure S1a show the slightly more flexible, by ~0.01 nm, chain configurations obtained for the juxtaposed model, reflecting the poorer contacts between the non-aligned chains on opposing faces. Increasing the separation between the surfaces results in a strong increase in chain fluctuations, with the less constrained chains exhibiting flexibilities twice that measured for the cramped chains at very short separations. The time-averaged 0.06 nm chain RMSF values at a separation of 4.4 nm are similar to those measured in free-standing monolayers, approximately 0.05-0.06 nm.[9-10] A similar trend of more flexible carbons at greater separations is seen for the methyl groups at the interface (Figure S1b).

The rationalization of computed interaction energies based on number, strength and type of interface contacts may be measured using interface density profiles, in addition to the RDF plots. The analysis of density profiles for the interaction between two nanoparticles (main text Figure 2) is given in Figure S2 below. The computed profiles for methyl group densities along the axis of inter-particle attraction shows how, in agreement with the RDF plots in Figure S1b and main text Figure 2b, the minimum energy inter-particle separation (Figure S1a and main text Figure 2a) is obtained when inter-chain contacts are optimised. These optimised contacts have significant van der Waals attractions between chains (and to a lesser extent, electrostatic attractions, given the low polarity of the alkyl C-H bonds) while avoiding repulsions associated with cramped/overlapping chain orientations. Such cramped, unfavourable interactions were found for nanoparticles that were squeezed together to sub-2 nm separations in the present study (main text Figure 2). The density profiles in Figure S2 show that the more favourable separations, with optimised chain contacts, are associated with a broad distribution of tightly packed (but not overlapping) methyl groups at the interface.
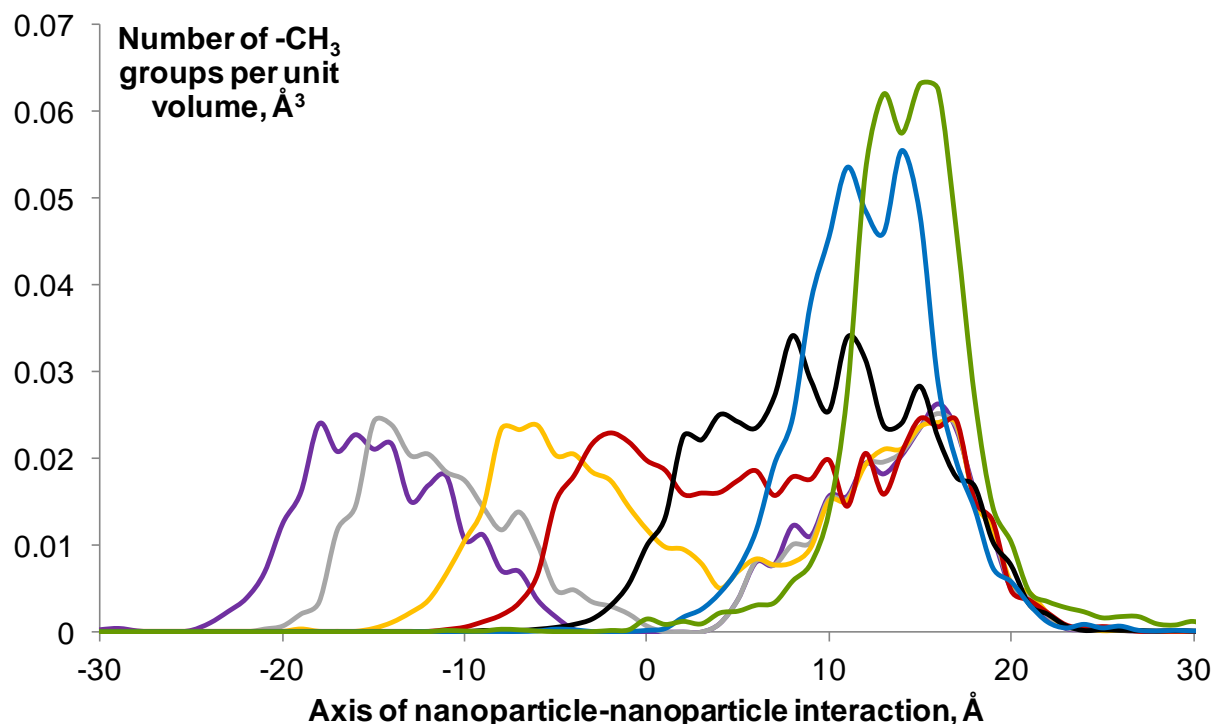
Figure S2. Computed density profiles of alkyl methyl groups along the axis of inter-particle attraction. The number of methyl groups counted in the plane parallel to the nanoparticle surfaces (using a bin size of 1 Å) is divided by the area of the interface (144 nm^2) to generate the 1-D density profiles of density of methyl groups per unit volume, Å^3. The curves are coloured according to separation using the same colour scheme as used in main text Figure 2, coloured from purple to green as the inter-particle gap is shortened, with data for the optimum 2.3 nm gap separation coloured black.

S2.2 Molecular dynamics of the interface between a coated surface and a bare surface: Figure S3a

shows the interaction profile for the interaction of a flat coated surface and a flat non-coated surface.

This bare, uncharged Au(111) surface slab serves as a model non-coated surface, with the alternative

interaction between two coated surfaces modelled above (Figure S1) and 30 nm particle interaction with

the coated surface modelled in the main text (Figure 4a). The optimum gold-gold gap separation is at 2.1

nm, which gives optimised monolayer-surface van der Waals contacts as shown in the radial distribution

functions in Figure S3b. The 2.1 nm separation provides the best balance of contacts around the target

force field H---Au separation of 0.236 nm.[2]

(a)

(b)
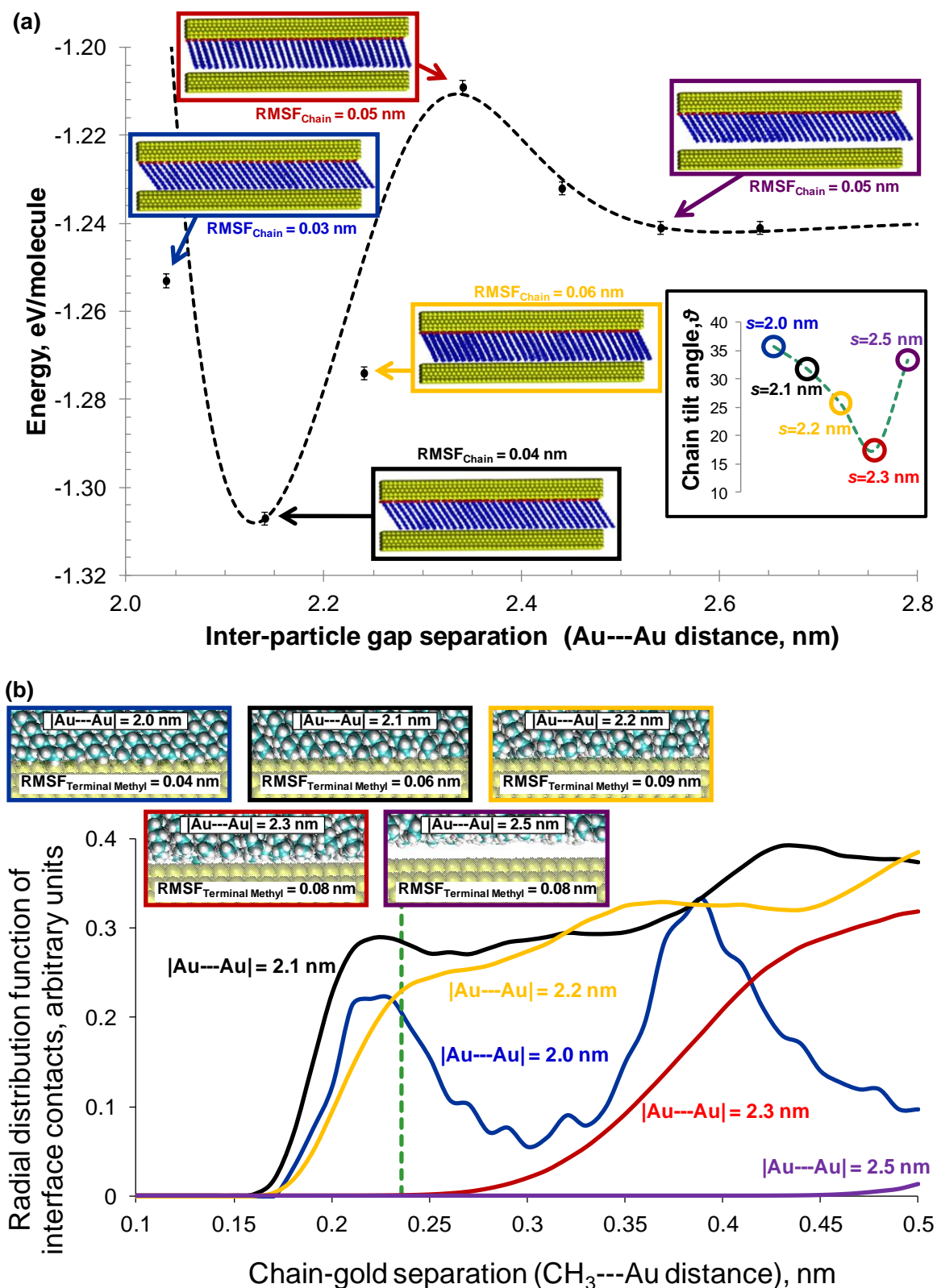
Figure S3. (a) Interaction profile for a coated flat surface and a bare surface. The inset lower righthand panel shows time-averaged chain tilt angles in the corresponding structures. **(b)** Radial distribution functions (RDF) for contacts between

terminal methyl groups and the bare Au(111) surface. In this case, the dashed green line marks the target 0.236 nm H---Au distance.[2] See Figure S1 legend for more details.

The shape of the particle-surface potential in Figure S3a is reminiscent of an AFM "pull off" curve.[11] The energy well at 2.1 nm is followed by a barrier between touching and non-touching regimes with a plateauing of the energy at larger separations towards that of an isolated monolayer,[9-10] approximately -1.24 eV/molecule. This is the same asymptotic value calculated above from Figure S1a for the interaction between two coated surfaces, and corresponds to the intramolecule packing on each of the (non-interacting) surfaces.

The distribution of time-averaged tilt angles as a function of the separation between the nanoparticle and the coated surface, is plotted in the lower righthand panel inset in Figure S3a. The tilt angles show that the maximum in the potential at 2.3 nm coincides with a significant untilting of the alkanethiol chains away from their preferred tilt angle of approximately 30°.[9-10,12-13] This low tilt angle of approximately 17° at 2.3 nm reflects the partial untilting of the chains into more extended orientations that attempt to retain the methyl-surface contact at the expense of inter-chain methylene packing.[14] The film regains the near-30° tilt at larger separations as the isolated monolayer geometry is restored. Likewise, the tilt angles increase and get closer to 30° as the separation decreases below 2.3 nm. Note the tilt at the computed optimum distance of 2.1 nm is very similar to the tilt in the isolated SAM (at s=2.5 nm). However, the highest (and noisiest) time-averaged tilt angle of 37° is found at the smallest (repulsive) separation of 2.0 nm due to slight crumpling of the chains in the restricted volume of this narrow interface.

Chain flexibilities in Figure S3a are similar to those measured for the coated surfaces in Figure S1a above. On the other hand, the terminal methyl carbon flexibilities in Figure S3b are intermediate between those given for the coated surfaces in Figure S1b and the 30 nm particles in main text Figure 2b. The RDF distribution shows again how the computed optimum separation is directed by maximisation of the population of optimum inter-chain separations. The RDF distribution in Figure 3b
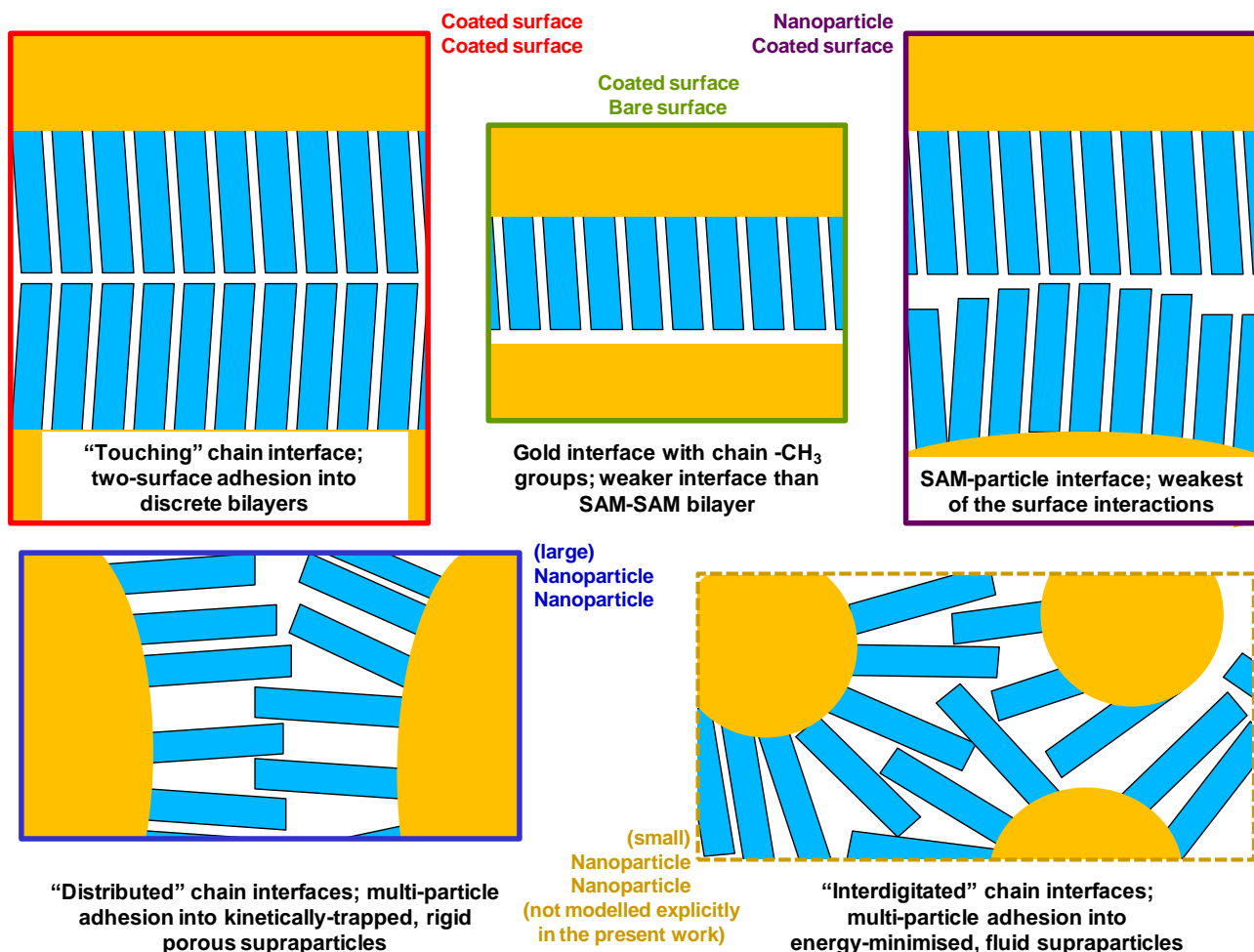
also reflects the intermediate strength interaction between the coated surface and the bare surface. The interaction is weaker than the highly ordered methyl stacking for the coated surfaces, but stronger than the interaction between the 30 nm particles. As shown in main text Figure 2b and Figure 3 the interaction between the two nanoparticles is distributed between interdigitated methylene, touching methyl and distant methyl arrangements. These three "zones" are encountered as one radiates outwards from the centre of the particle-particle interface.

The computed energy *vs*. separation profile in Figure S3a also reflects this intermediate strength nanoparticle-surface interaction (main text Figure 4b). The energy minimum in Figure S3a corresponds to -1.3 eV per chain, compared with better (-1.4 eV) and worse (-1.1 eV) chain energies in Figure S1a and main text Figure 2a for the coated surfaces and 30 nm particles. Finally, the penalties for deviation away from the minimum in the interaction profile between the coated surface and bare surface are as expected very steep in the absence of the interfacial chain-chain interactions. The 0.3-0.5 eV/nm chain penalties computed from Figure S3a are 2-3 times and 30-50 times higher, respectively, than those computed for the interaction between two coated surfaces (Figure S1a) and two coated particles (main text Figure 2a).

S2.3 Further discussion of nanoparticle interaction strengths and types of supraparticle assemblies: The relative strengths of the different potentials for different interaction types, as plotted in main text Figure 4b, may be rationalised on the basis of the local concentration of alkyl molecules at the interface. This population of interacting chains at each interface determines the strength of the individual chain-chain interactions. These are "distributed" between long-range very weak interactions, medium strength methyl-methyl *touching* interactions and very strong *interdigitated* interactions, as sketched in Figure S4 below. This concentration of alkyl molecules in turn depends on the curvature of the interacting faces; hence the potentials in main text Figure 4b show weak chain-chain interaction between large nanoparticles, intermediate strength interaction between large nanoparticles and surfaces and

(relatively) strong interaction between surfaces. Figure S4 sketches these alternative interfaces and illustrates also the very strong interaction between small nanoparticles,[15,16] due to the high number of interfaces and high concentration of interacting chains in each interface, which gives a very high driving force for supraparticle assembly.

Coated surface
Coated surface

Coated surface
Bare surface

Nanoparticle
Coated surface

"Touching" chain interface; two-surface adhesion into discrete bilayers

Gold interface with chain -CH₃ groups; weaker interface than SAM-SAM bilayer

SAM-particle interface; weakest of the surface interactions

(large) Nanoparticle Nanoparticle

"Distributed" chain interfaces; multi-particle adhesion into kinetically-trapped, rigid porous supraparticles

(small) Nanoparticle Nanoparticle (not modelled explicitly in the present work)

"Interdigitated" chain interfaces; multi-particle adhesion into energy-minimised, fluid supraparticles

Figure S4. Schematic of the interfaces formed involving surfaces (top) and those involving only nanoparticles (bottom), with boxes coloured using the same scheme as for the potential curves in main text Figure 4b. For the large nanoparticles (bottom left), chain contacts are distributed into interdigitated, touching and weak longer-range interactions. The cartoon for the small nanoparticles is based on literature data, *e.g.*, refs 15-16, and is supported by meso scale Brownian dynamics simulations performed at elevated temperatures (see Figure S5 and supporting text, below).

The main difference relative to the assembly of supraparticles from large nanoparticles as modelled in the present study is that small nanoparticles retain self-correction at the full-nanoparticle level,[17] allowing the individual nanoparticles to rotate and move to more thermodynamically stable, high-coordination sites in the assembling supraparticle by (presumably) optimizing all chain-chain

interactions. In contrast, larger nanoparticles form large-area interfaces with chain-chain interactions distributed between interdigitated chains, touching terminal methyl groups and very weak longer-range interactions (see main text Figure 3 and discussion in the main text). While the individual chain-chain interactions remain weak, the crucial difference for large *vs.* small nanoparticles is that the high chain populations result in tightly-bound, large-area interfaces. In other words, the deep interaction wells (summed over all interacting chains in the large-area interfaces), coupled with the short range of the interactions compared to the size of large nanoparticles, inhibits nanoparticle-level self-correction. Hence, the growing cluster of nanoparticles does not crystallise/precipitate like a typical Lennard-Jones system into ordered supraparticles but rather (we predict) the clusters ripen into porous supraparticles.

More regularly-shaped supraparticles could be obtained under experimental conditions which decrease the interaction well depths by, *e.g.*, (a) choosing a solvent which will interfere with and buffer the alkyl-alkyl hydrophobic interaction between nanoparticles, or (b) using elevated temperatures to weaken the inter-particle attraction. More simulations and experiments should be performed over a range of different nanoparticle shapes and sizes to investigate the dependence of the supraparticle shape and porosity on the nanoparticle curvature. Such future work may aid the discovery of the critically large nanoparticle size at which local, chain-level self-correction becomes insufficient to provide nanoparticle-level self-correction. At this critically large nanoparticle size, self-healing of the clusters into non-porous supraparticles should be deactivated and kinetic control switched on.

To summarise the above rather detailed explanation for the sketches shown in Figure S4, we believe that two effects are in operation which determine the nature of the assembly:

1) the strength of the interaction between the chains (interdigitated > touching > separated)

 2) the number of chains that interact

For small nanoparticles there is strong interaction that includes significant interdigitation, but the population of chains at each interface is small. Hence, while the depth of the energy minimum per chain

will be relatively deep, the total energies are still comparable to thermal energies ($k_B T$) and hence nanoparticle-level rearrangements to the thermodynamically most stable high-coordination states are possible.

For larger nanoparticles, while there is also some interdigitation at the smallest gaps, the amount of interdigitation is far less than for small nanoparticles (due to the decreased curvature of large nanoparticles). The majority of the chains are well separated from each other, so the energy per chain has quite a shallow minimum. Crucially however, the interactions are additive and so, summing over the large number of chains at each nanoparticle-nanoparticle interface gives a huge driving force for interface formation. Finally, for two coated planes the amount of interdigitation approaches zero, but all the chains are at the same, relatively close distance and the well depth per chain is then stronger than for large particles. Hence, we find that at the molecule-level, the smaller the nanoparticle the stronger the interaction but, on the other hand, the small particles can rearrange themselves at the nanoparticle-level, because the total nanoparticle-level interaction is weaker for small nanoparticles.

As a first step towards modelling assembly with weaker interaction strengths, we modelled the change in supraparticle properties as the effective temperature T* (see section S1.2) is raised. This corresponds, to a first approximation, to assembly of nanoparticles in the presence of progressively weaker interaction strengths. As discussed above, interaction strengths may be tuned experimentally by changing nanoparticle type, shape, coating, solvent type, dielectric, pH, *etc*. Hence, in order to assess the role of the depth of the potential energy well, we have studied the aggregation process of 30 nm nanoparticles in a wide range of temperatures, scaling T* = $k_B T$ / $\varepsilon_{NP\text{-}NP}$ from 0.001 up to 5.0 (equivalent to changing the interaction energy from 25 to 0.005 eV at a fixed T.) The simulations were terminated when the system reached the equilibrium, but not before 15 million steps of Brownian dynamics.

Panels a-c of Figure S5 show root mean square fluctuations (RMSF, ρ_i) in nanoparticle positions in the supraparticles assembled using Brownian dynamics at three different effective temperatures, and

measured over long trajectories of well equilibrated systems. Values of ρ_i corresponding to the maximum values of such histograms were plotted against the temperature T* (panel d). A logarithmic plot (inset) revealed linear correspondence and was used to obtain parameters of a power function (red dashed line). The resulting function is plotted in green in the right panel of the Figure, and shows a square root type dependence of nanoparticle root mean square fluctuation on temperature, as expected from the Einstein diffusion equation (section S1.2). Finally, panel e of Figure S2 shows that the volume fraction occupied by nanoparticles decreases nearly monotonically at higher temperatures due to the thermal agitation.

Taken together, these control simulations at higher temperature indicate that at elevated temperatures the columnar growth mode (discussed in the main text for the strongly interacting nanoparticles) becomes unstable and the system becomes more fluid-like, more dynamic, and easier to compress. We find that the structures easily reorganize when the gravitational field is applied. Hence it is clear that supraparticle assembly is more fluid at higher temperatures, indicating the shift from a very sticky regime to a more fluid regime. The sticky regime (see also cartoon in Figure S4) has nanoparticles interacting very strongly with each other and hence becoming kinetically trapped in low-coordination sites to make a porous supraparticle, while the more fluid regime allows the nanoparticles to move more freely and find optimum sites to make a tightly-packed, thermodynamically favored supraparticle.[17] The present simulations indicate that the more fluid regime becomes operational for clustering of large 30 nm diameter nanoparticles under experimental conditions that weaken the interaction potentials, which may include the use of a good solvent and/or elevated temperatures, and the simulations also indicate that care should be taken to avoid functionalising nanoparticles with very strongly interacting coatings (*e.g.*, ssDNA coats with complementary base pair sequences that give multi-site electrostatic stabilizations in water) to avoid unintentionally forming porous assemblies.
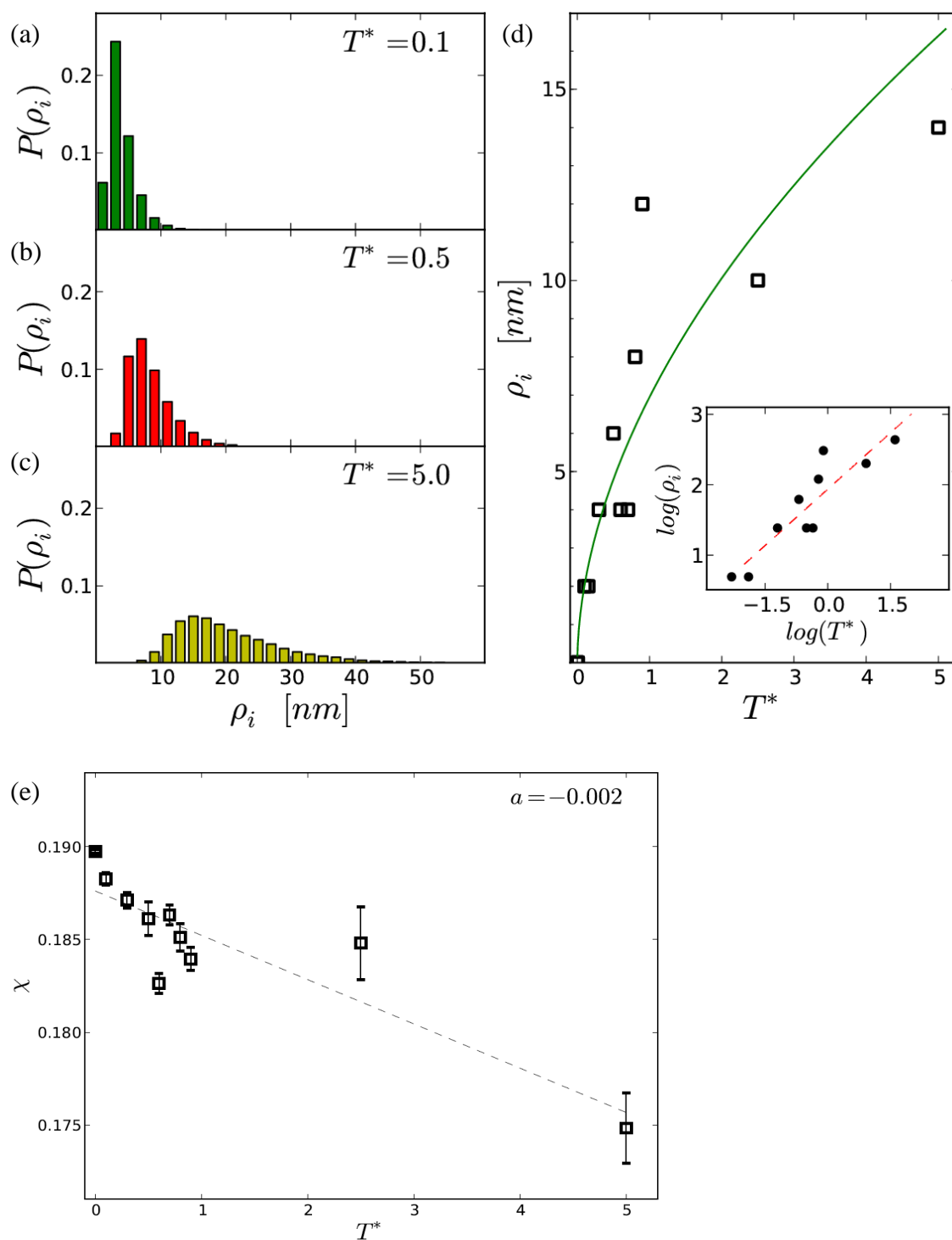
Figure S5. Panels a-c show histograms of nanoparticle root mean square fluctuations ρ_i in supraparticles assembled at effective temperatures T* 0.1, 0.5 and 5.0 respectively. In the calculations we did not take into account events of NPs moving to the neighboring simulation box, via periodic boundary conditions. Such events, even at higher temperatures were rare and thus did not introduce significant errors beyond a small tail in the distributions. Panel d plots the ρ_i(max) values against T* over a large range of temperatures, with the log-log relation given in the inset plot. Panel e plots the volume fraction χ occupied by nanoparticles as a function of T*.

S3 – Extracting supraparticle surface roughness from meso scale simulations

To quantify surface roughness from the coarse-grained structures, each nanoparticle is represented by 160 points located on its surface. The points are then placed within a grid in which the lattice constant is set to the nanoparticle diameter. For each grid cell, the z coordinate of the topmost point is selected as representing the local surface elevation, with the elevations plotted along the x-direction in Figure S6 for two selected values of y. The surface roughness parameter is determined as the root mean square deviations in these elevations across the whole x-y plane.

The greater vertical disorder observed at the repulsive wall compared with the attractive wall at the monolayer coverage (main text Figure 5) propagates to higher elevations at larger coverages. For the structure shown in main text Figure 6b, the characteristic level of roughness is 60.9 nm. When the substrate becomes repulsive, the roughness grows to 62.5 nm.
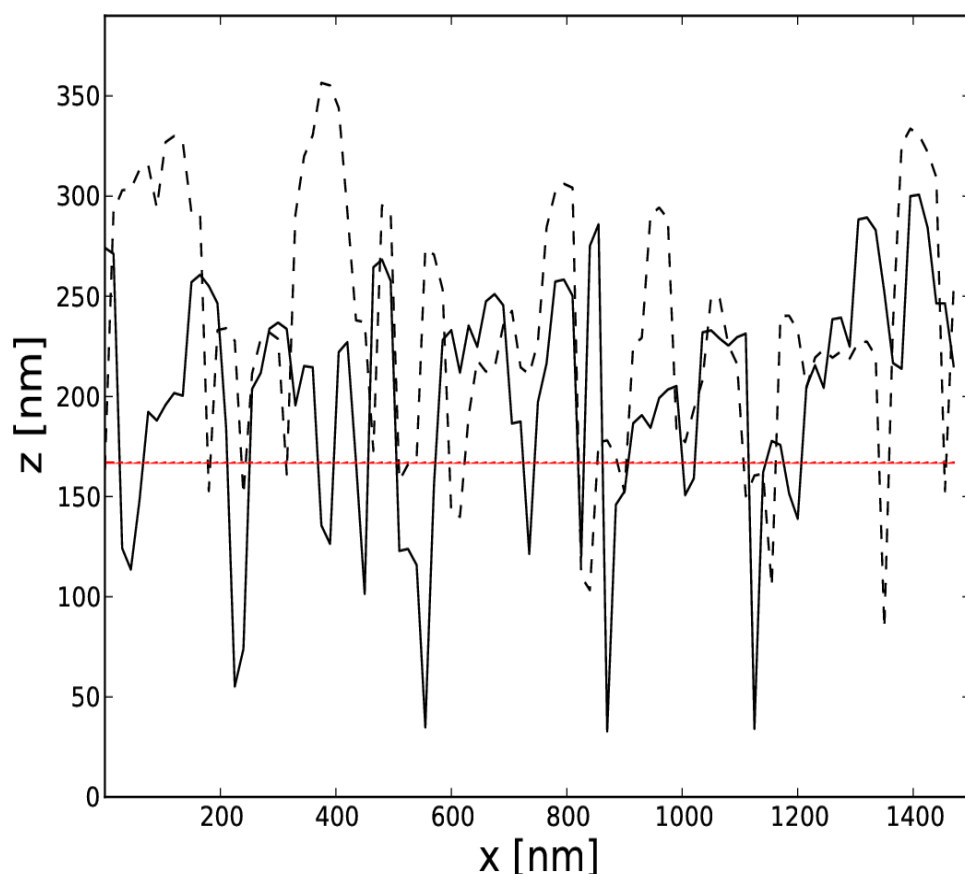
Figure S6. The top surface elevation of the structure along the x-direction projection for two selected values of y (the dotted and solid lines), from main text Figure 6. The mean elevation is indicated by the solid horizontal line, and is equal to 165 nm.

S4 –Calculation of supraparticle coalescence *via* aggregative sedimentation of nanoparticles

Figure S7 shows representative structures computed from simulations of particle coalescence (as described in the main text), with different values for column separation S and column width a. One of the most interesting structures identified using this procedure is given in main text Figure 7.
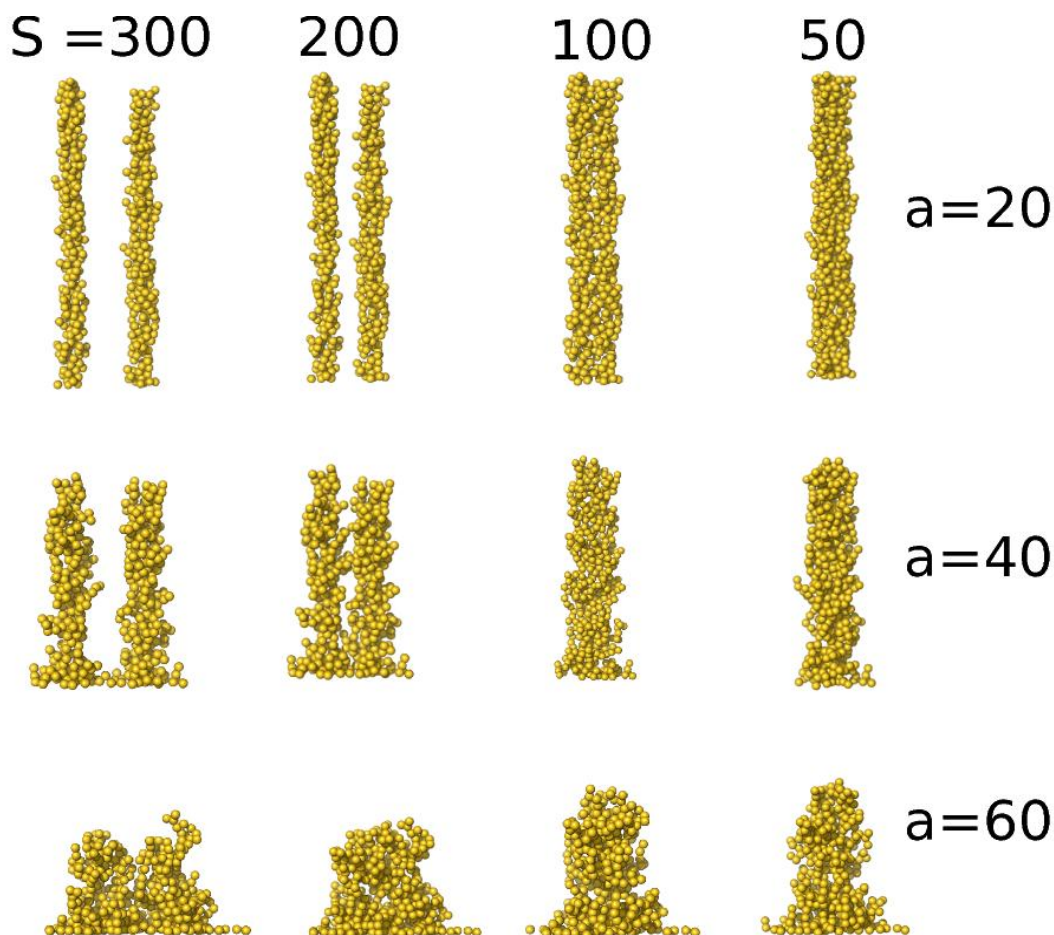
Figure S7. Aggregative sedimentation of 500 nanoparticles effusing from two sources placed above the attractive wall. S is the separation between the two sources and a is the characteristic width of effusion.

References

1.   T. Darden, D. York and L. Pedersen, *J. Chem. Phys.*, 1993, **98**, 10089-10092.

2.   A. D. MacKerell, D. Bashford, M. Bellott, R. L. Dunbrack, J. D. Evanseck, M. J. Field, S. Fischer, J. Gao, H. Guo, S. Ha, D. Joseph-McCarthy, L. Kuchnir, K. Kuczera, F. T. K. Lau, C. Mattos, S. Michnick, T. Ngo, D. T. Nguyen, B. Prodhom, W. E. Reiher, B. Roux, M. Schlenkrich, J. C. Smith,

R. Stote, J. Straub, M. Watanabe, J. Wiorkiewicz-Kuczera, D. Yin and M. Karplus, *J. Phys. Chem. B*, 1998, **102**, 3586-3616.

3.   J. C. Phillips, R. Braun, W. Wang, J. Gumbart, E. Tajkhorshid, E. Villa, C. Chipot, R. D. Skeel, L. Kale and K. Schulten, *J. Comput. Chem.*, 2005, **26**, 1781-1802.

4.   O.A. von Lilienfeld and D. Andrienko, *J. Chem. Phys.*, 2006, **124**, 054307.

5.   F. F. Abraham and Y. Singh, *J. Chem. Phys.*, 1977, **67**, 2384-2385.

6.   D. L. Ermak and J. A. McCammon, *J. Chem. Phys.*, 1978, **69**, 1352-1360.

7.   K. A. Dill, S. Bromberg and D. Stigter, *Molecular driving forces : statistical thermodynamics in chemistry and biology*, Garland Science, New York ; London, 2003.

8.   J. C. Love, L. A. Estroff, J. K. Kriebel, R. G. Nuzzo and G. M. Whitesides, *Chem. Rev.*, 2005, **105**, 1103-1169.

9.   G. Gannon, J. A. Larsson, J. C. Greer and D. Thompson, *Langmuir*, 2009, **25**, 242-247.

10.   G. Gannon, J. C. Greer, J. A. Larsson and D. Thompson, *ACS Nano*, 2010, **4**, 921-932.

11.   A. L. Weisenhorn, P. Maivald, H. J. Butt and P. K. Hansma, *Phys. Rev. B*, 1992, **45**, 11226-11232.

12.   P. Fenter, P. Eisenberger and K. S. Liang, *Phys. Rev. Lett.*, 1993, **70**, 2447-2450.

13.   M. D. Porter, T. B. Bright, D. L. Allara and C. E. D. Chidsey, *J. Am. Chem. Soc.*, 1987, **109**, 3559-3568.

14.   S. Vemparala, B. B. Karki, R. K. Kalia, A. Nakano and P. Vashishta, *J. Chem. Phys.*, 2004, **121**, 4323-4330.

15.   Y. Lalatonne, J. Richardi and M. P. Pileni, *Nat. Mater.*, 2004, **3**, 121-125.

16.   P. Schapotschnikow, R. Pool and T. J. H. Vlugt, *Nano Lett.*, 2008, **8**, 2930-2934.

17.   Y. S. Xia, T. D. Nguyen, M. Yang, B. Lee, A. Santos, P. Podsiadlo, Z. Y. Tang, S. C. Glotzer and N. A. Kotov, *Nat. Nanotechnol.*, 2011, **6**, 580-587.